JOURNAL OF GEOPHYSICAL RESEARCH, VOL. 102, NO. B9, PAGES 20,287–20,304, SEPTEMBER 10, 1997

Detailed structure of the top of the melt body beneath the East Pacific Rise at 9°40′N from waveform inversion of seismic reflection data

J. S. Collier and S. C. Singh

Bullard Laboratories, Department of Earth Sciences, University of Cambridge, Cambridge England

Abstract. We have applied waveform inversion to multichannel seismic reflection data collected at the East Pacific Rise at 9°40′N in order to determine the precise velocity structure of the magma body causing the axial magma chamber reflection. Our analysis supports the idea of a molten sill as previously suggested from forward modeling of seismic data from this location. Our inverted solution has a 30-m-thick sill with a P wave seismic velocity of 2.6 km s^{-1}. Although not well constrained by the data we believe that the S wave velocity in the sill is not significantly different from 0.0 km s^{-1}. The low P- and S wave velocities in the sill imply that it contains less than 30% crystals. The molten sill is underlain by a velocity gradient in which the P wave velocity increases from 2.6 to 3.5 km s^{-1} over a vertical distance of 50-m. The shape of our velocity-depth profile implies that accretion of material to the roof of the sill is minor compared to accretion to the floor. The underlying velocity gradient zone may represent crystal settling under gravity. We suggest that only material from the 30-m-thick layer can erupt.

Introduction

During the last 10 years there have been a number of detailed geophysical studies aimed at determining the distribution of melt within the crust beneath fast spreading ridge axes. The East Pacific Rise (EPR) near 9°N was chosen as one of the sites of study following an earlier discovery of a bright seismic reflector beneath the ridge axis here which was interpreted as the roof of an axial magma chamber, the AMC reflector [*Herron et al.*, 1980]. In 1985 a conventional multichannel common-depth point reflection (CDP) and two-ship expanding spread profile (ESP) experiment was conducted at 9°N [*Detrick et al.*, 1987; *Mutter et al.*, 1988; *Kent et al.*, 1990, 1993a,b; *Vera et al.*, 1990], which was followed in 1988 by a complementary ocean-bottom seismometer tomography experiment [*Toomey et al.*, 1990, 1994]. The current geophysical model of melt distribution in the crust at this location taken from *Kent et al.* [1993a] is shown in Figure 1. In the model the AMC reflector represents a thin layer of pure melt (P wave velocity, Vp =3.0 km s^{-1}; S wave velocity, Vs =0.0 km s^{-1}) which overlays a zone of partially solidified crystal mush ($Vp >$ 3.0 km s^{-1} and $Vs >$0.0 km s^{-1}). The width of the AMC reflector and hence that of the magma body is well constrained [*Kent et al.*, 1990, 1993a] and varies between 0.25 and 4.15 km beneath different parts of the ridge axis. The thickness of the sill, however, has not to date been well constrained. *Kent et al.* [1993a] argue that the lack of a distinct reflector below the AMC reflector (or "basal" reflector) could be due to the sill being less than a seismic wavelength thick such that the reflection from its base interferes with the reflection from its top. With the available data they show that a sill only 10–50-m-thick is consistent with this observation (see their Figure 22). However, they also acknowledge that the lack of a basal reflector could be due to a gradient zone beneath the molten layer. The work presented here follows on from that of *Kent et al.*, [1993a] in which we look in greater detail at the AMC waveform with the aim of better constraining the structure at the top of the magma chamber. The thickness of the melt sill has important implications to the dynamics within the chamber and volcanic processes at the axis.

Data

The data used in this study (Figure 2) is taken from the 1985 experiment [*Detrick et al.*, 1987]. Our analysis assumes a one-dimensional structure, and so we use data from the along-axis line CDP 41 near its intersection with cross-axis line CDP 29. This location is about 10 km north of ESP 5 midpoint that is used to constrain the long to medium-scale velocity structure. This location was chosen as the bathymetry of this part of the ridge is approximately linear (hence minimizing two dimensional (2-D) topographic effects) and the axial magma chamber (AMC) reflector is ro-

Paper number 97JB01514.
0148-0227/97/97JB-01514$09.00

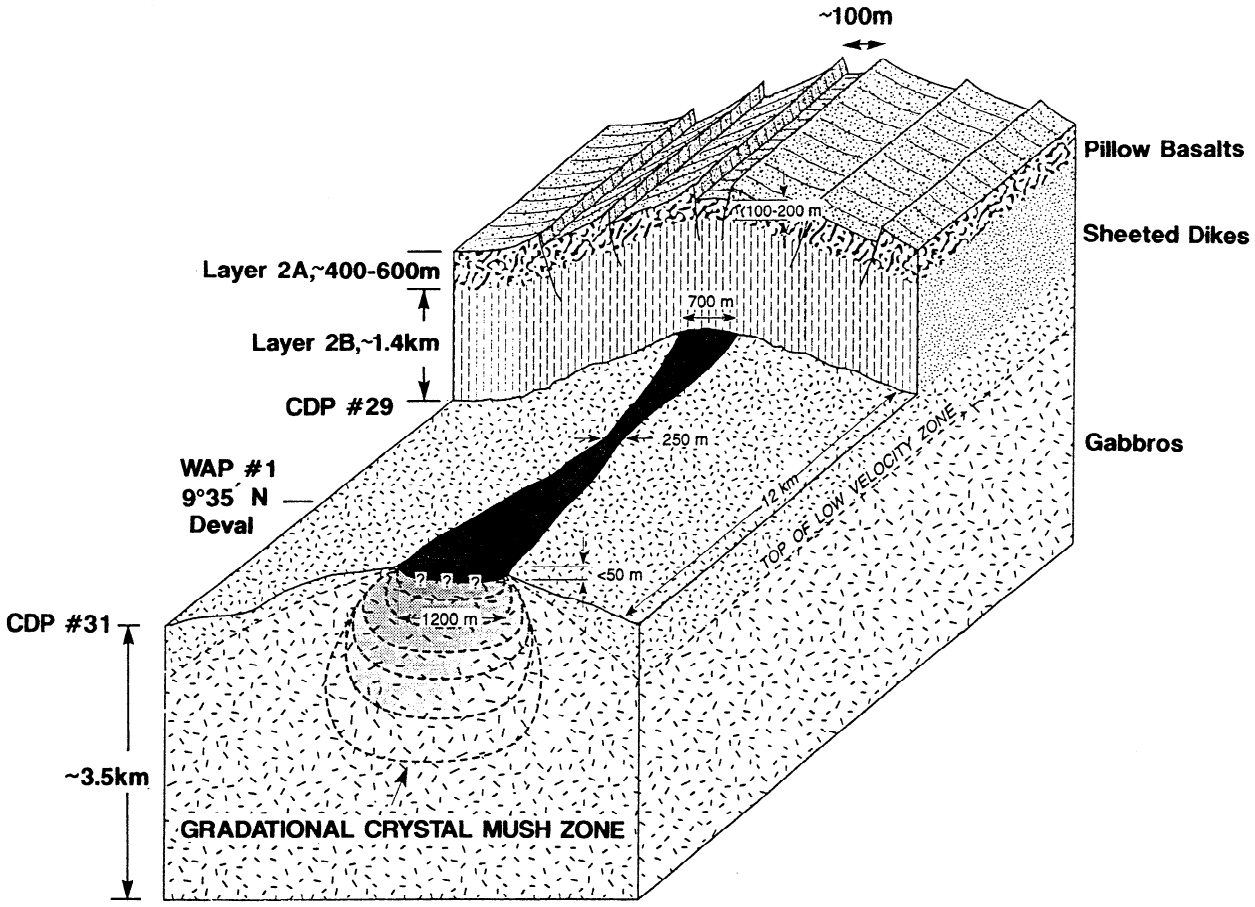

Figure 1. Cartoon of crustal structure at the East Pacific Rise near 9°N from *Kent et al.* [1993a]. The magma chamber consists of a thin, mostly molten sill (black) overlying a region of partial melt (shaded). In this study we determine the detailed structure at the top of this low-velocity zone. Locations of conventional (CDP) and wide-aperture (WAP) across-axis seismic profiles are marked.

bust (700-m wide) and centrally crossed by line CDP 41 here (this is not true for the part of line CDP 41 at the ESP 5 midpoint [*Kent et al.*, 1993a]). The data were collected with a 2.4-km-long, 48-channel streamer with a minimum offset of 0.35 km and receiver spacing of 0.05 km. The data were sampled every 4 ms in time, and a 62-Hz antialias filter was applied at acquisition. The source was a tuned 4-gun array totalling 30 L, towed at 10 m depth, and fired every 50 m. To increase signal-to-noise ratio, a supergather was made by stacking 55-fold constant offset traces. This supergather is shown in Figure 3a. The AMC reflection is seen at ~4.05 s two-way travel time (TWT). The amplitude of this reflection falls below the signal-to-noise level at a range of about 2 km. Figure 4 shows the frequency spectrum of the data. The AMC contains frequencies in the range of 5-35 Hz.

Our analysis is performed in the delay time-slowness ($\tau - p$) domain for computational efficiency and accuracy. We used a 3-D $\tau - p$ transform performed in the frequency domain as described by *Harding* [1985] and implemented by *Korenaga et al.* [1997]. A 3-D $\tau - p$ transformation maintains waveform accuracy required for waveform inversion but suffers from more serious artifacts than a simple 2-D slant stack [*Kappus et al.*, 1990]. Two artifacts of particular concern in this data set arise from (1) truncation effects, due to limited spatial aperture and (2) spatial aliasing. To alleviate truncation effects, we interpolated four traces inward from the innermost trace and applied a cosine taper to the innermost and outermost five traces. Spatial aliasing effects, which arise from large trace spacing, can originate from small slownesses (positive slope) or from large slownesses (negative slope). The former can be alleviated by using a weighting filter [*Singh et al.*, 1989], and the latter can be alleviated by using the Hankel function instead of the Bessel function for larger slownesses [*Harding*, 1985]. We did not correct for source and receiver directivity (which discriminates against waves with large slowness) because of the relatively small slownesses used in this study. As the $\tau - p$ transform in effect performs an integration of the data, the $\tau - p$ data were differentiated to make the frequency spectrum compatible with the time domain source wavelet. Figure 3b shows the $\tau - p$ transformed data. Note that the low slowness traces are comparatively noisy (particularly at small τ) due to remnant aliasing effects, so we used a minimum slowness of

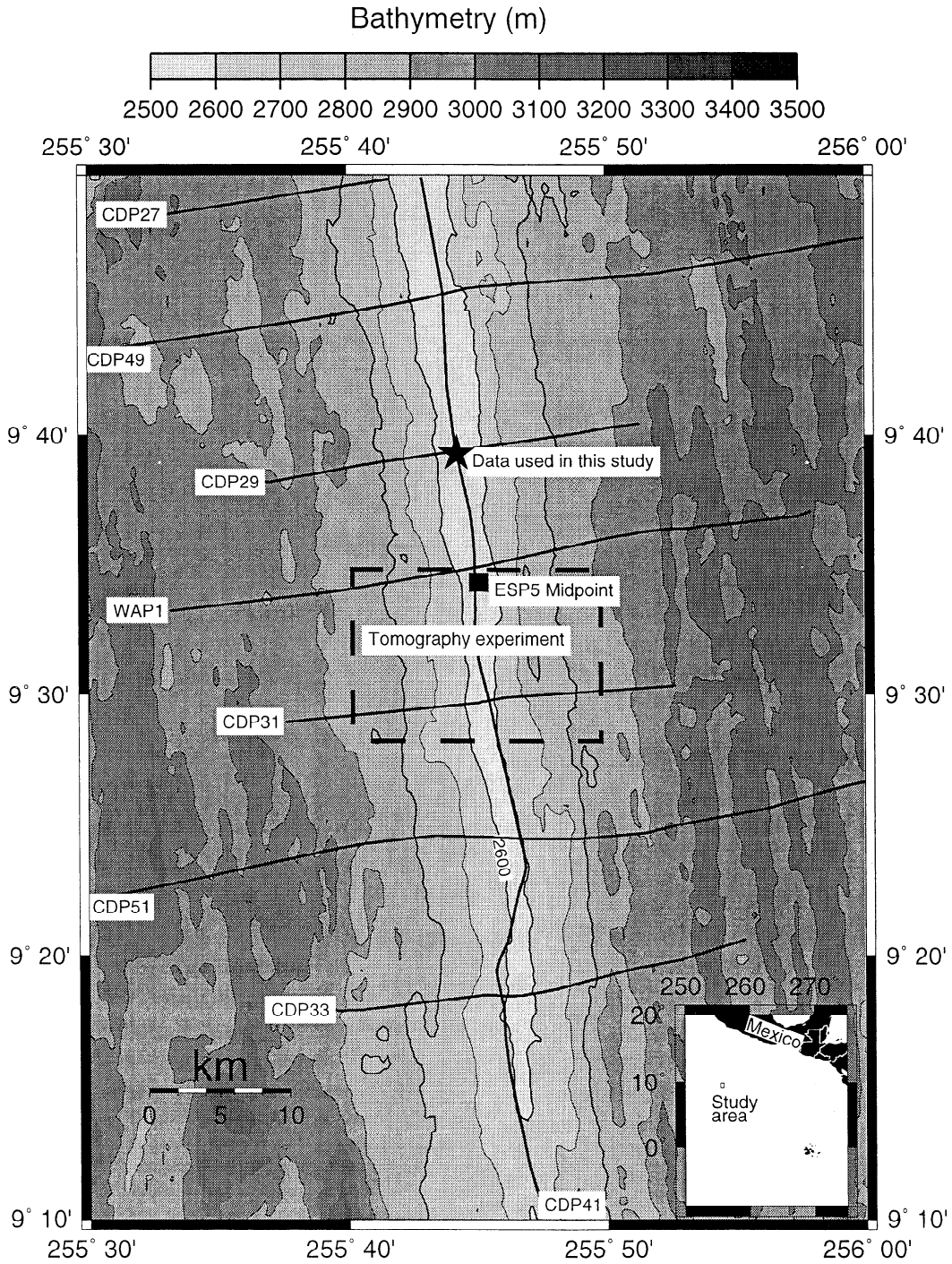

Figure 2. Bathymetric map of the East Pacific Rise showing locations of CDP profiles collected during the 1985 experiment. The location of the supergather of the along-axis line CDP 41 used in this analysis is shown with the star, and the midpoint of ESP 5 used for the long wavelength velocity profile is shown with the square. The dashed box shows the location of the 1988 tomography experiment [*Toomey et al.*, 1990]. The section of ridge between 9°45′ and 9°52′ erupted in 1991 [*Haymon et al.*, 1993].

0.02 s km^{-1} in our analysis. The maximum slowness that can be used with confidence is 0.1 s km^{-1}.

Previous Models

We subjected the previously proposed models of the AMC at this location to our method of synthetic seismogram computation to assess their fit. The model of *Vera et al.* [1990] was derived from reflectivity forward modeling of ESP 5. In their model the form of the low-velocity zone was not well constrained. They model the AMC with a 180-m-thick pure melt (Vp =3.0; Vs =0.0 km s^{-1}) underlain by a partial melt zone where Vp and Vs gradually increase with depth. This model produces synthetics with amplitudes that are too small for the onset of the AMC reflection but match the later

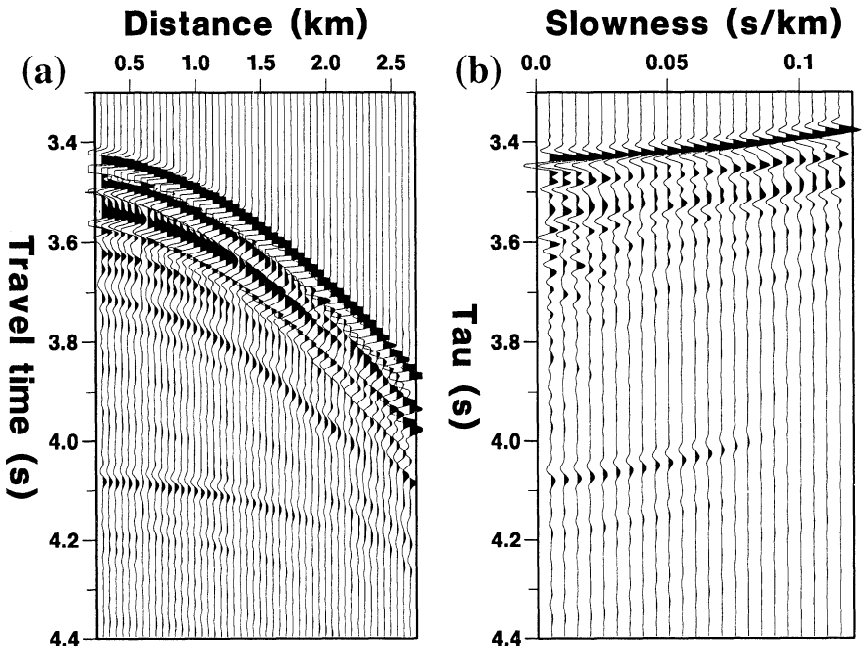

Figure 3. (a) Supergather (55-fold constant offset stack) of CDP line 41 in time-offset $(t - x)$ domain. The AMC (the reflection from the top of the magma chamber) is at 4.08 s TWT at near offset. (b) Supergather in slowness-intercept $(\tau - p)$ domain.

part of the waveform reasonably well (Figure 5a). Furthermore, this model also predicts a 180° phase shift at 0.08 s km^{-1} slowness which is not seen in the data. A second model of the AMC at 9°N was proposed by *Kent et al.* [1993a]. Their model was devised by forward modeling (based on the method of *Kennett* [1983]) of the same supergather used in this study (but in the distance travel time domain). In the *Kent et al.* [1993a] model (hereinafter referred to as the Kent model) the velocity structure from the seafloor to the top of the melt sill is identical to the *Vera et al.* [1990] model (hereinafter referred to as the Vera model). However, in the Kent model the material beneath the melt sill has the same properties as the material above, so the mostly molten material forms an isolated sill rather than a capping layer as in the Vera model. In the Kent model the thickness of the sill can vary between 10 and 50 m. We tried models with a melt sill of 10, 20, 30, 40 and 50-m-thick (Vp =3.0 km s^{-1}) and found the 50-m-thick model to give the best overall fit (Figure 5b). Numerically, the Kent model gives an overall poorer fit than the Vera model (it has a slightly larger misfit). In the Kent model, reflections from the base of the sill constructively interfere with the reflections from the top of the sill giving a better fit to the amplitude of the early part of the AMC compared to the Vera model, although the waveform shape does not match as well. Also note how despite having the same Vp and Vs contrast at the top of the sill as the Vera model the synthetics do not show the unwanted phase shift of the Vera model. None of the Kent models that we tried produced the required amplitudes for the whole of the AMC waveform. We therefore proceeded to improve the fit by the application of waveform inversion.

Waveform Inversion

Seismological studies (including that of *Vera et al.* [1990] and *Kent et al.* [1993a]) commonly employ forward modeling techniques using trial and error methods, with selection or rejection of models being made by visual comparisons of synthetic and real seismograms. The problem with forward modeling is that it is essentially subjective (i.e., is open to the bias of the interpreter), and a complete error analysis is not achievable. Inverse methods automate the trial and error approach of forward modeling and therefore make the velocity

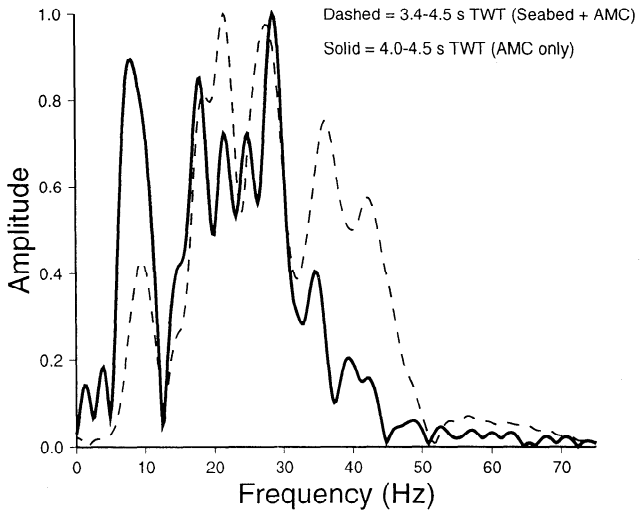

Figure 4. Frequency-amplitude spectra. The dominant frequency in the AMC reflection is between 5-35 Hz which corresponds to 20-250-m vertical resolution.

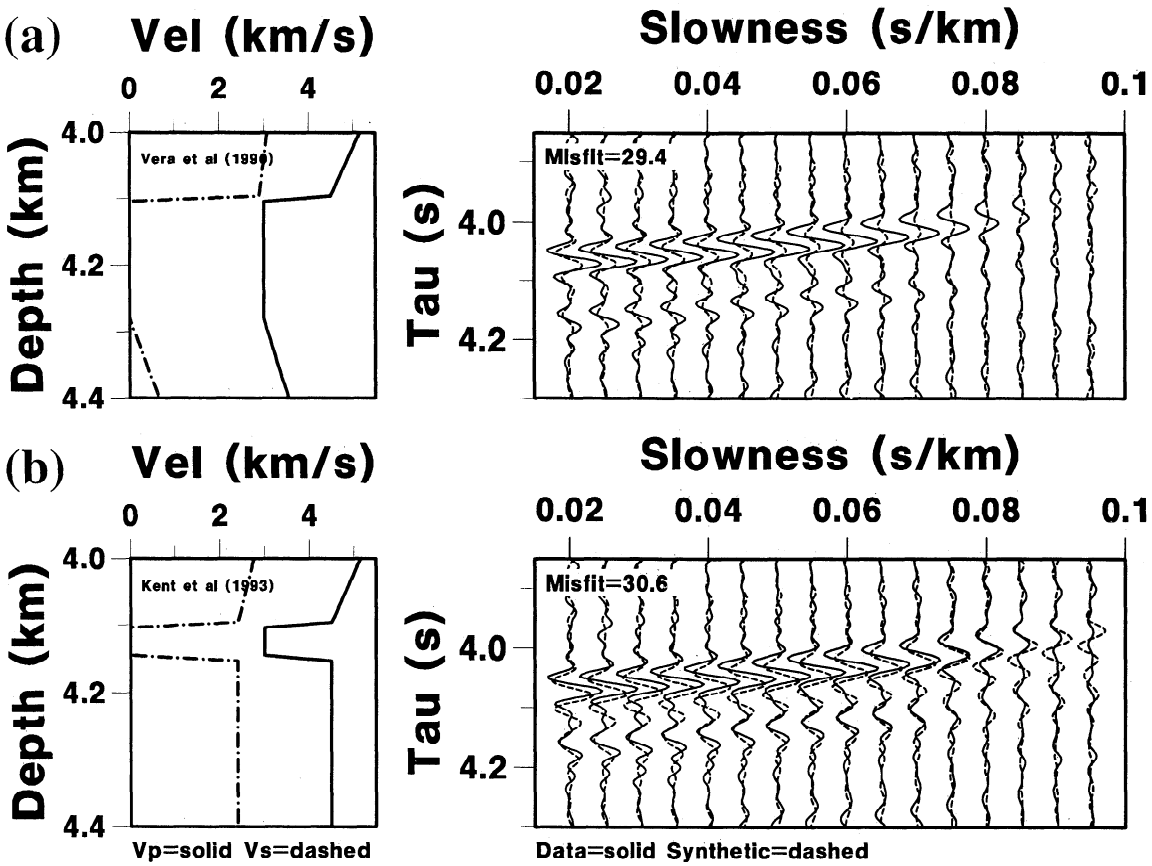

Figure 5. Assessment of the fit of previously proposed models for the melt lens at the top of the chamber. (a) *Vera et al.* [1990] and (b) *Kent et al.* [1993a] 50-m-thick sill model. Misfits are in arbitrary units and should be used only to assess the comparative fitness (as it depends on the number of traces together with the time and frequency windows used in its calculation). The synthetics were generated with the source Wavelet D of Figure 8.

estimation more robust, accurate, and less interpreter dependent. Waveform inversion consists of minimizing the difference (misfit) between observed and synthetic seismograms, sample by sample. The disadvantage of waveform inversion is that it attempts to fit all parts of the waveform equally, whether it be real, noise or artifact. Meaningful inversion therefore needs the skills of an interpreter to extract the desired (real) components from the resulting velocity model.

A schematic flow chart of our inversion procedure is given in Figure 6. We calculated synthetic seismograms for a horizontally layered model using the generalized reflection transmission matrix method [*Kennett and Kerry*, 1979]. This method accurately treats multipathing and mode conversions. The input model defines P wave velocity (Vp), S wave velocity (Vs), density (ρ), P wave attenuation (Qp) and S wave attenuation (Qs) for a stack of isotropic, elastic layers. We chose a layer thickness of 8 m with reference to the minimum wavelength present in the data. Our inversion procedure was to minimize the misfit function using a conjugate-gradient method [*Kormendi and Dietrich*, 1991]. The misfit function for waveform is highly nonlinear, that is, it contains numerous local optima. We therefore needed to test various starting models to maximize the likelihood of finding the global minimum (the unique "best

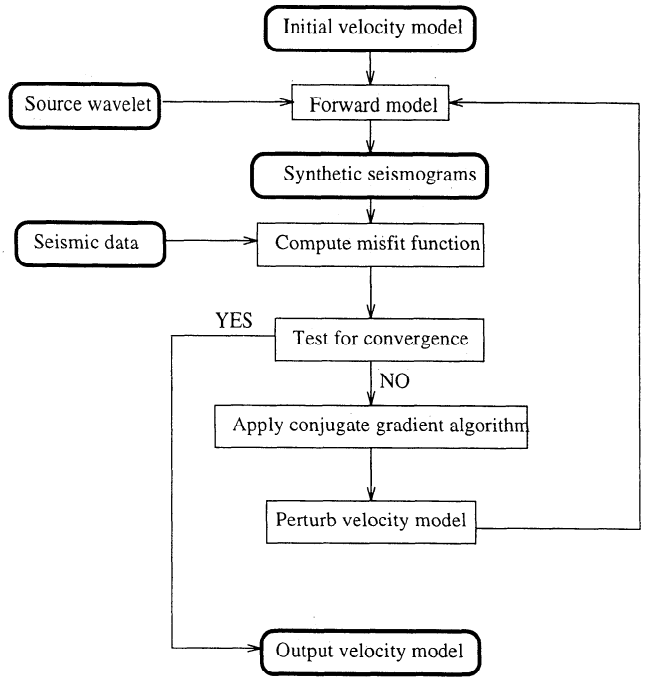

Figure 6. Schematic flow chart of the seismic waveform inversion procedure applied in this study.

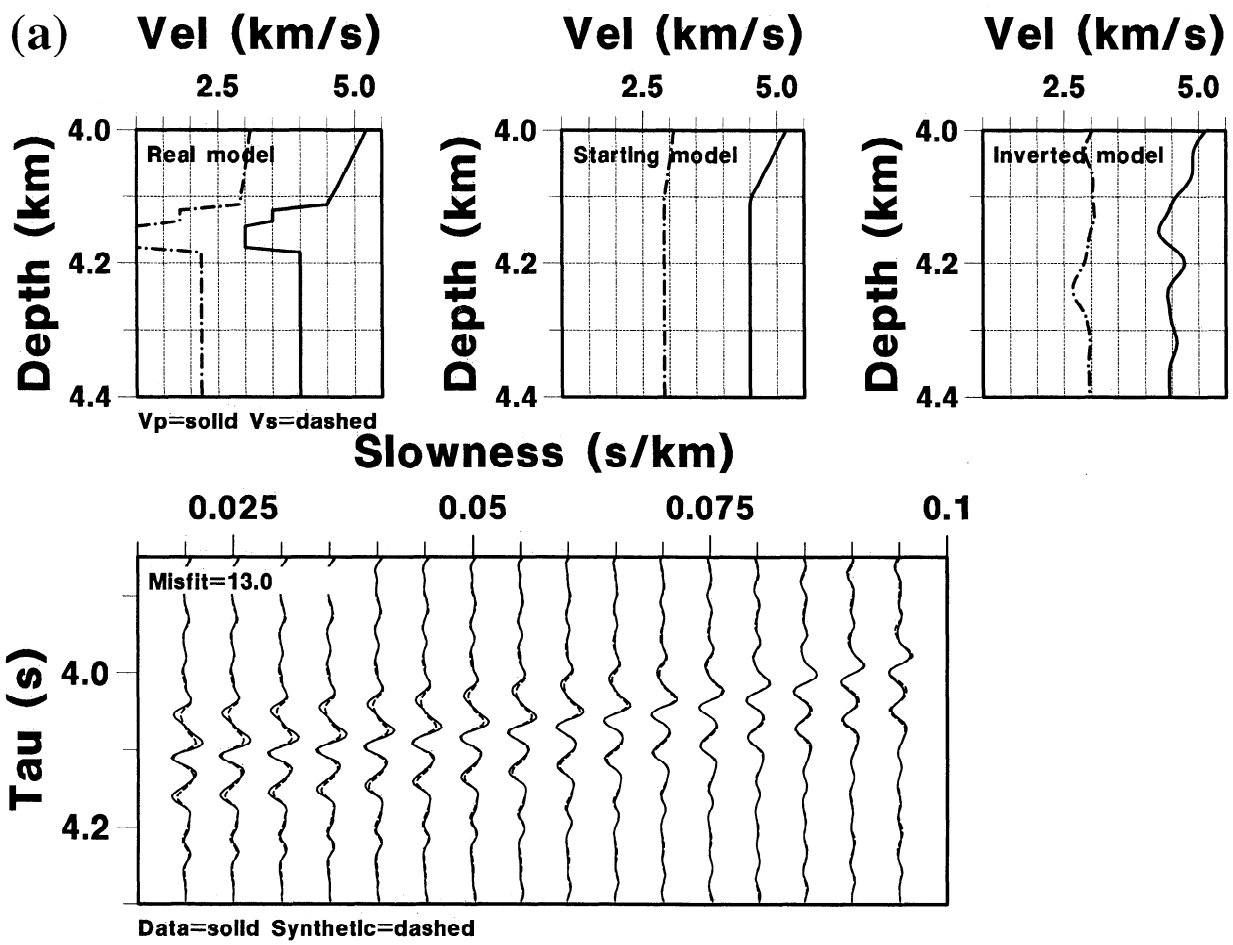

Figure 7. Synthetic inversion tests using the source wavelet and slowness window appropriate for this experiment. We show results for a model with two velocity steps of 20 and 40-m inverted from two different starting models (a and b). Note the effect of the starting model on the inverted model and the lack of resolution of Vs .

fit" model). This method has been successfully applied to a number of different geological targets [e.g., *Singh et al.*, 1991; *Minshull and Singh*, 1993; *Singh et al.*, 1993].

Before proceeding with the waveform inversion of the real data we ran some synthetic examples in order to investigate the dependence between the inverted model obtained and various input features. In these models we generated synthetic seismograms from a known velocity structure and then attempted to invert for it from a given starting model. In different tests we varied AMC structure in the real model (we kept the upper structure identical throughout) and the form of the starting model. We used a slowness window and source wavelet appropriate for the 1985 EPR experiment throughout.

We needed to make a decision about which model parameters were allowed to change during the test inversions. For an elastic isotropic medium the seismic wave propagation can be described by Vp, Vs and ρ. Coupling between these parameters for real materials introduces problems for multiparameter inversion. This problem is discussed by *Tarantola* [1986], who suggests inverting for the different parameter types sequentially, in order of decreasing importance. Fortunately, laboratory measurements of bulk seismic velocity and density for basaltic melts at different temperatures suggest that the three parameters are not strongly coupled [*Murase and McBirney*, 1973]. These experiments also show that ρ changes little during melting (less than 10%) compared to large changes in Vp (up to 60%) and Vs (up to 100%). We therefore adopted a scheme in which we inverted first for Vp and then for Vs (with no inversion for ρ). A second decision we needed to make was whether to use different slowness and frequency subsets in successive runs of a particular inversion. *Kormendi and Dietrich* [1991] recommend optimizing for Vp by considering low slownesses (precritical) first and then progressively include contributions from the high slowness (nearcritical and postcritical) to optimize for Vs. *Minshull and Singh* [1993] further recommend opening out the frequency window during the inversion. After a number of trials we concluded that in our narrow slowness and frequency band there was no gain in adopting such schemes, so we inverted for all slownesses and frequencies simultaneously.

The results of our synthetic tests served to emphasize the intrinsic limitations placed on inversion of band- and range-limited data and the importance of the starting model (a consequence of the nonlinearity of the misfit function). We show two of our test results in Figure 7 and discuss key features below.

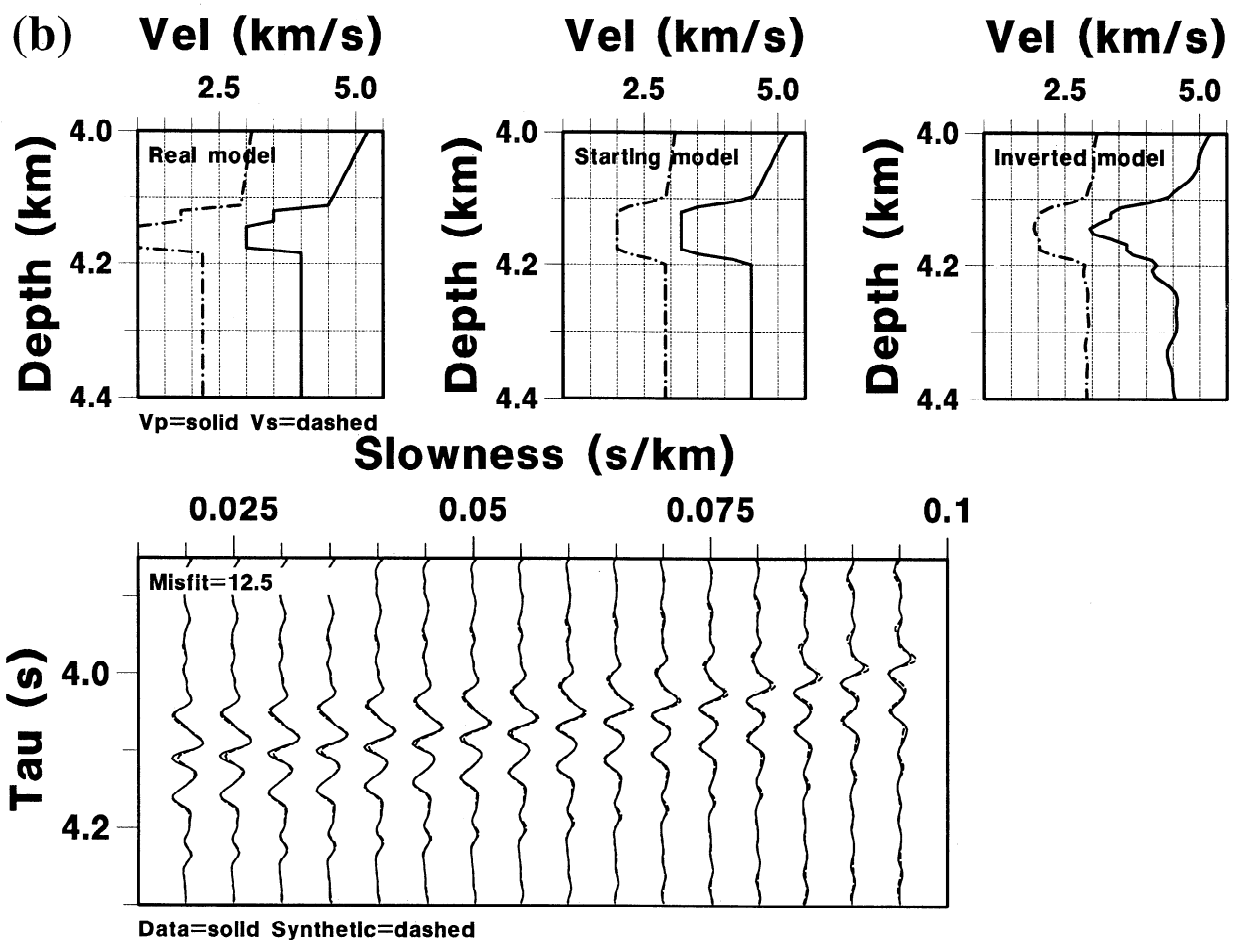

Figure 7. (continued)

Band limited data. Real band-limited sources restrict our ability to resolve a sharp interface (first-order discontinuity). Such an interface needs a white source (one in which all frequencies are evenly represented) to be resolved perfectly, and in the case of a band-limited source it will generate side lobes when inverted such that it appears "smeared" . This effect is clearly seen in all our results by the "wavy" nature of the inverted models. An additional consideration is the wavelength of structure that can be extracted from a given bandwidth. For the AMC reflection the signal is in the 5–35 Hz band, which at a velocity of 3.0 $\mathrm{km\,s^{-1}}$ places a theoretical lower limit on vertical resolution ($\lambda/4$) of 20–150 m. Our tests showed that with our source wavelet we can resolve well structure of length scales between 20 and 100 m, and to a lesser extent structure above 100 m. We were unable to resolve structure with length scales more than 200 m.

Slowness window. As our data contain only pre-critical slownesses of P wave reflections, we do not expect Vs to be well constrained. This was amply demonstrated in our tests in which we were unable to recover Vs structure (Figure 7). Therefore for the real data we chose to invert for Vp only, but substitute different physically viable, Vs values to compare the results. We also ran different Vp inversions with different ρ and Qp values to assess their control on our results.

Starting model. The classical shortcoming of iterative gradient methods is the importance of the starting model [*Kormendi and Dietrich*, 1991]. Our tests, however, showed that even when the starting model is far from the real model the inverted solution showed features that enabled a refined starting model to be generated which led to a significant lowering of the misfit. For example, Figure 7a shows results with minimum information in the starting model yet the inversion correctly predicts the width of the low-velocity zone and hints that it may be multilayered. Introducing a low-velocity feature into the starting model (Figure 7b) results in an inversion result close to the correct solution and produces synthetic seismograms that visually fit the data better. In other tests we introduced features into the starting model for which we had no evidence, and these generally had a strong detrimental effect on the inversion solution. We concluded that when inverting the real data the testing of a range of starting models was essential to enable the global minima to be reached. The strong influence of the starting model makes it difficult to quantify model resolution based on a posteriori covariance matrix. However, we estimate that errors are of the order ± 8 m and ± 0.2 $\mathrm{km\,s^{-1}}$ in depth and velocity.

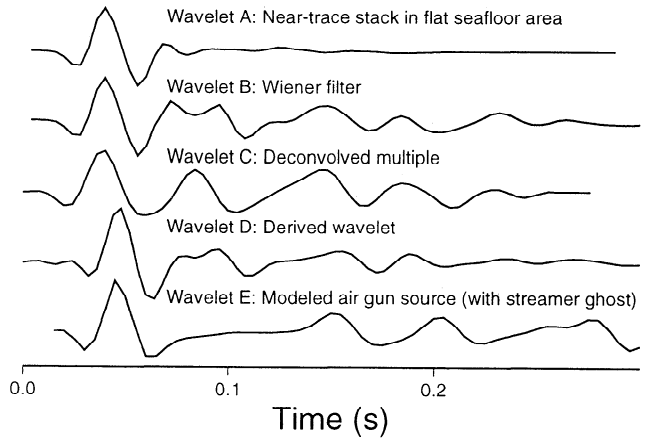

Figure 8. A comparison of estimates of the source wavelet. See text for details.

Inversion Setup

Source Wavelet

A potential cause of error in our inversion is the estimation of the source wavelet (strictly the downward-directed energy pulse generated by the air gun array as recorded by an individual hydrophone). As seismograms are a convolution of the source with the reflectivity series (the velocity model we seek to obtain), errors in the source wavelet will map directly into errors in the final model. It is rare in seismic experiments to measure the far-field response of the air gun signature directly [*Ziolkowski*, 1991] nor have a robust estimate of the response of the hydrophones. To make matters worse, the signal recorded is also strongly influenced by variations in the towing depth (bubble pulse period and ghosts) and orientation (directivity effects) of both individual guns within the array and streamer. This experiment was no exception to the usual practice, and so we need to estimate the source wavelet.

For a marine source it is important that the source wavelet used is of sufficient length to include all bubble pulses of amplitude greater than the ambient noise level. We used the following five different methods to estimate the source wavelet. The results can be compared in Figure 8. Note that the first three require assumptions about the near-surface structure.

1. Perform a near-offset stack over a region of relatively flat seafloor which is thought to most closely approximate to a half-space velocity discontinuity (i.e., it is not underlain by secondary reflectors within the desired time length of the extracted wavelet). This was done for line 41 (G. M. Kent, personal communication, 1996) and is Wavelet A of Figure 8. Note that this was the wavelet used in the study of *Kent et al.* [1993a].

2. Design a Wiener filter from the reflectivity series by assuming the velocity model. The upper-crustal structure of zero-age oceanic crust is quite well known and generally agrees with that shown in Figure 10, namely, that layer 2A is approximately a homogeneous unit, with P wave velocity of $\sim$2.4 km s^{-1} just $\sim$400-m-thick (equivalent to 80 ms TWT) which overlays a steep velocity gradient within which velocities in excess of 5 km s^{-1} are reached in a few hundred meters or less [*Vera and Diebold*, 1994]. Our Wiener filter which produced such a reflectivity series, designed from the first five traces of the $t - x$ gather, is Wavelet B of Figure 8.

3. Deconvolve the seafloor multiple reflection with the seafloor primary to get the reflectivity response of the seafloor, then design an inverse filter of the reflectivity and convolve the result with the seafloor primary to get the source wavelet. In terms of equations this assumes

$$\text{seabed} = s \star r \star f \tag{1}$$

$$\text{multiple} = -s \star r \star r \star f \tag{2}$$

where s is the source function, f is the instrument response, r is the seabed reflectivity and the star is a convolution (we want $s \star f$). This was performed on move-out corrected low τ traces and is Wavelet C of Figure 8.

4. Derive the wavelet from the data by taking the average spectra within a time window to produce the wavelet spectrum. The phase was set to minimum and the result was transformed into the time domain. This wavelet was determined by using the fact that the phase and log magnitude amplitude spectra are Hilbert pairs [*Oppenheim and Schafer*, 1975, p. 345]. This has the advantage that it assumes nothing about the near-surface structure and has been shown successful at recovering known source wavelets (R. Hobbs, personal communication, 1996). It was performed on low slowness $\tau - p$ traces and is Wavelet D of Figure 8.

5. Forward model the air gun response [*Laws et al.*, 1990]. This was performed for the Conrad air gun array assuming a gun depth of 10 m and streamer depth of 12 m. The result was band pass filtered 0–40 Hz and is Wavelet E of Figure 8.

We were encouraged by the similarity of our source wavelets estimated from the different procedures. We note that the near-offset stack (Wavelet A) stands out from the others in having a much smaller bubble pulse to primary/ghost amplitude. We suggest that this could be due to underlying structure invalidating the simple half-space assumption required for this method of estimation. The bubble trail is as important as the primary/ghost package in the inversion. Our preferred estimate is Wavelet D as it requires no assumption about the velocity structure or equipment configuration. To test the validity of the wavelets we ran forward and inverse models with the *Vera et al.* [1990] upper crustal structure (Figure 9). In the forward models the bigger bubble pulse of Wavelet D produces a better fit to the data than Wavelet A. Further, when this model was inverted with Wavelet D the result was stable with only few modifications being made to the starting model. In comparison, inversion with Wavelet A was unstable and resulted in an effect that we interpret as missing bubble pulse energy directly mapping into the model. The misfit for Wavelet A is also significantly larger than the misfit for Wavelet D. On this basis we selected Wavelet D for all future work.

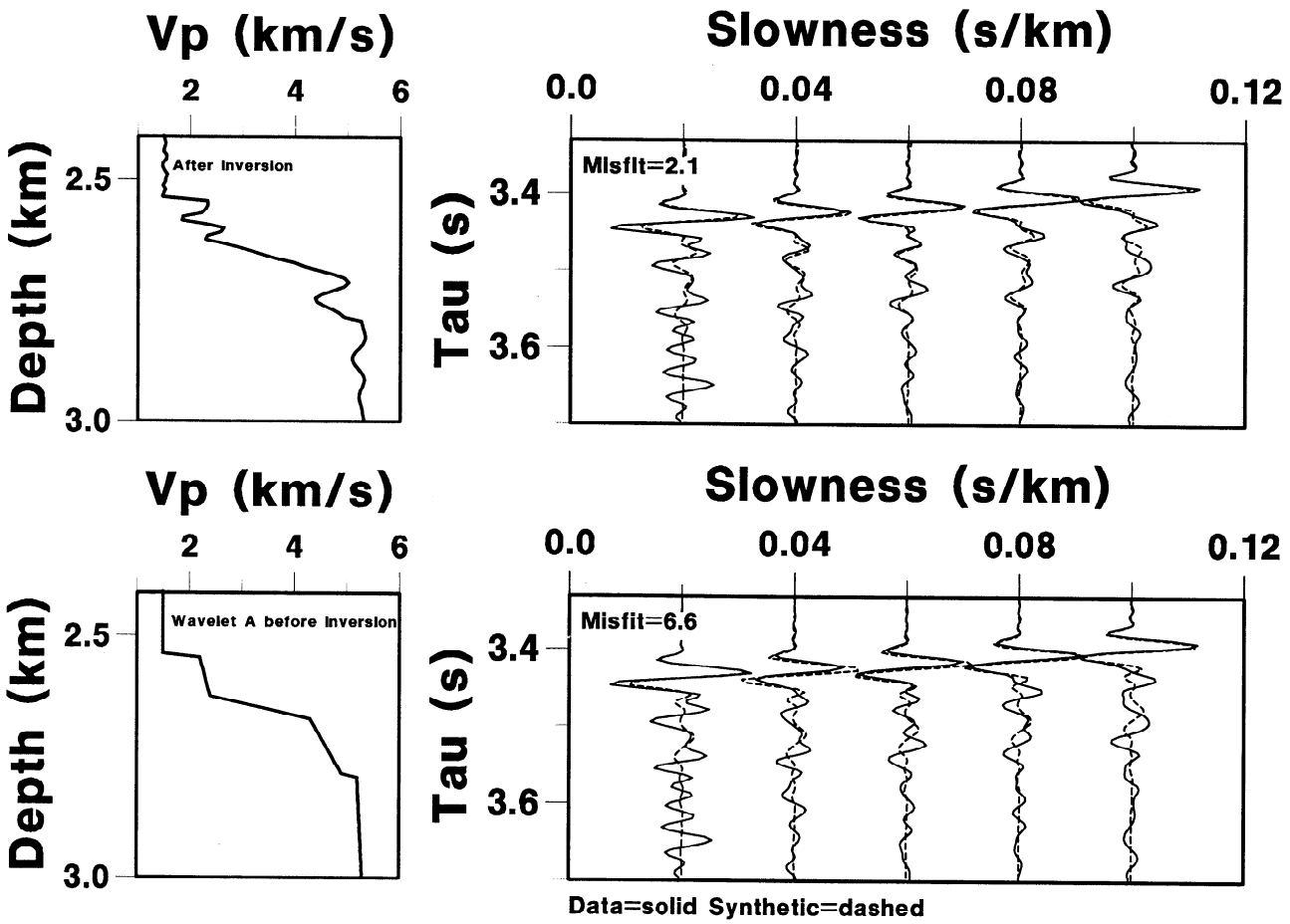

Figure 9. A comparison of forward modeling and inversion results of the upper crust with Wavelet A and Wavelet D of Figure 8.

Starting Model

Before running any inversions of the real data we tested the applicability of our chosen starting model taken from the ESP results of *Vera et al.* [1990] to our particular near-normal incidence data. The result is shown in Figure 10. Note that throughout our analysis we scaled the source wavelet such that the peak-to-peak amplitude of the seabed reflection matched that of a synthetic generated with a model in which the seafloor P wave velocity is 2.2 $\mathrm{km\,s^{-1}}$. The fit of the synthetics to the data is good except for the waveform of the AMC itself. This model, however, correctly predicts the $\tau - p$ envelope of the AMC. We conclude that both the starting model for the upper crustal structure (above 3.8 km depth) and the source wavelet were acceptable.

The form of the negative velocity gradient immediately above the AMC (3.8-4.05 km depth) in the Vera model warrants some comment. Clearly, the absolute P wave velocity above the reflector will directly influence the P wave velocity determined for the material below. The ESP model is constrained to a depth of 3.8 km below sealevel (equivalent to 3.9 s TWT) by crustal diving rays which attain a maximum phase velocity of 6.25 $\mathrm{km\,s^{-1}}$. Below this the wide-angle reflection equivalent to the AMC requires the average velocity to be 5.5 $\mathrm{km\,s^{-1}}$ to the reflector. The form of the low-velocity zone was otherwise not well constrained by the ESP data, and in the Vera model the velocity inversion consists of a linear gradient where Vp falls from 6.25 to 4.5 $\mathrm{km\,s^{-1}}$ below which a first-order velocity discontinuity responsible for the AMC reflector at near-normal incidence occurs. The existence of this velocity inversion above the AMC has significant implications to the thermal and hydrothermal system at the axis and so *Toomey et al.* [1994] investigated it further using the tomography data collected in 1988. Unfortunately, they show that the tomographic data are insensitive to the precise form of the velocity-depth gradient just above the AMC, but they do require a velocity drop of at least 0.5 $\mathrm{km\,s^{-1}}$. We looked for resolution of this gradient in the CDP data (see below).

We proceeded to test various starting models of the AMC. We show a selection of the results in Figure 11. These particular inversions were run for 16 iterations and with a slowness window of 0.02–0.075 $\mathrm{s\,km^{-1}}$ and frequency band 2–35 Hz. Within this slowness window, Vs has negligible effect on the reflected P wave amplitudes and therefore it can be ignored. Misfits in arbitrary units are shown for each inverted (dashed) model in the top corner of each plot. The misfits are calculated for the whole seismograms (i.e., include mismatching

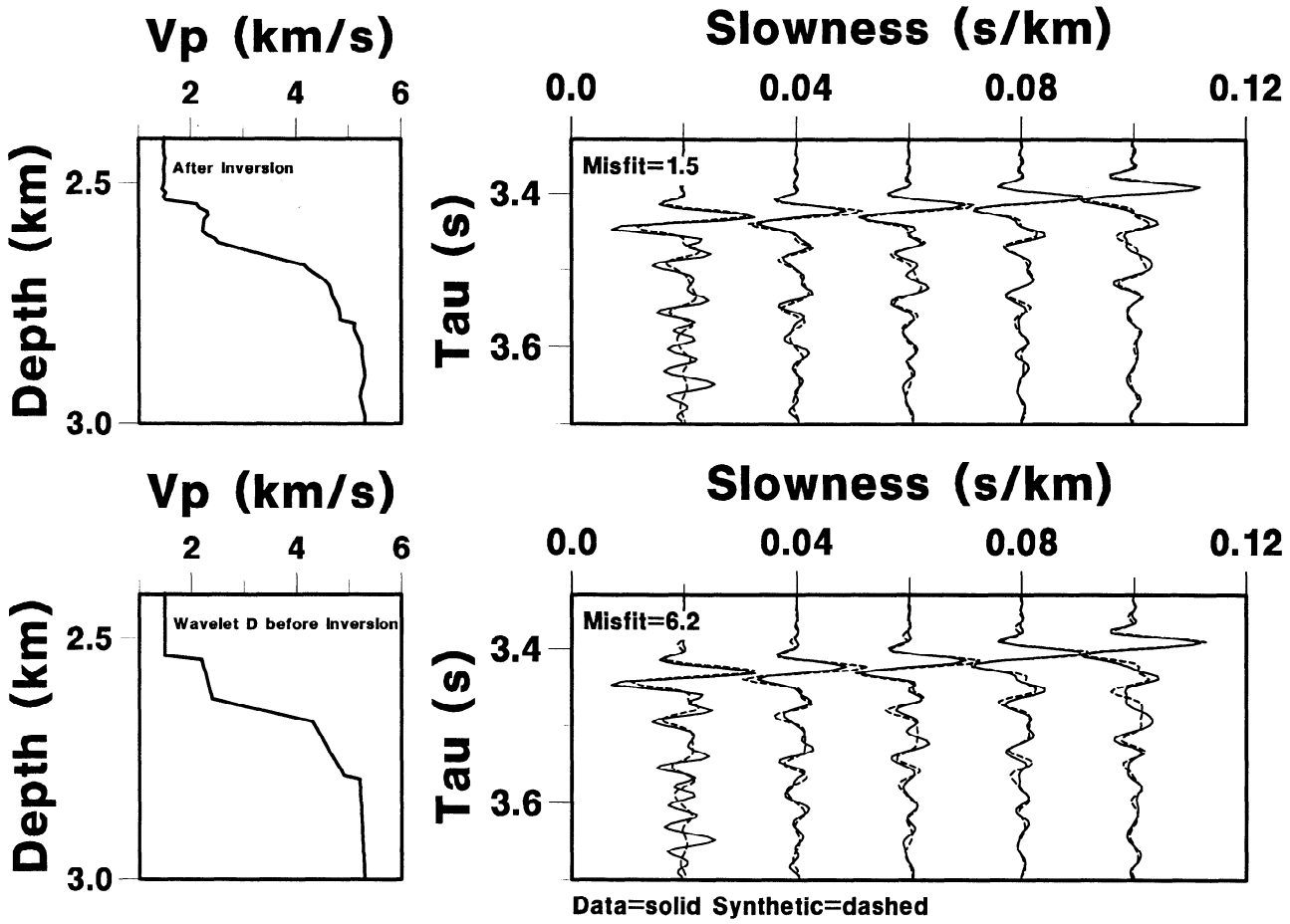

Figure 9. (continued)

upper crustal reflectivity) but as the only difference between the starting models is the structure of the AMC region, the relative misfit values indicate the goodness of fit of the low-velocity zone. We have subdivided the various starting models into a number of different criteria from which we make conclusions about the form of the low-velocity zone.

1. Velocity gradient above the AMC. We tested a number of different starting models with different linear negative velocity gradients above the AMC (Figures 11a- 11c). A Vp of 4.5 km s^{-1} immediately above the AMC (Figure 11c) was slightly preferred. We therefore used this in subsequent models.

2. Velocity gradient at the AMC. A starting model without any AMC structure generates a low-velocity layer 50–100 m thick (Figure 11f). We also tested starting models with gentle velocity gradients at the top of the AMC (Figures 11d and 11e), and all inversions tended to steepen the gradient but resulted in relatively large misfits. We concluded that the onset of the AMC reflector coincides with a rapid drop in Vp in less than 20 m vertical distance.

3. Evidence for a sill. We tried many models based on the sill-like Kent model (Figures 11g-11i). These models suggested that the sill was less than 50-m-thick.

4. Melt seismic velocity. Models with different melt and floor rock velocities (Figures 11j-11l) suggested that at the top of the sill there is a Vp drop of between 1.5 and 2.0 km s^{-1} and that at the base of the sill there is a smaller velocity increase (such that the floor rocks have a lower Vp than the roof rocks).

5. Velocity gradient beneath the AMC. Starting models with a velocity gradient below the AMC (rather than a first order discontinuity) produced slightly smaller misfits (Figures 11m-11o). There is no resolution in the data of structure more than 100 m below the AMC roof.

On the basis of this testing we chose to proceed with starting model o.

Results

Our preliminary inversions described above suggested that Vp at the top of the AMC is in the range 2.5–3.0 km s^{-1}. Such values lie on the part of the basalt melting curve where Vs changes rapidly as 100% melting is approached [*Murase and McBirney*, 1973]. We therefore chose to run a number of inversions of our chosen starting model but with different S wave velocity in the melt. These inversions were run for 24 iterations and with a slowness window of 0.02–0.1 s km^{-1} and frequency band of 2–35 Hz. To regularize the solution the model variance of 1.0 and the data variance of 0.25 [*Kormendi and Dietrich*, 1991] were used during the inver-

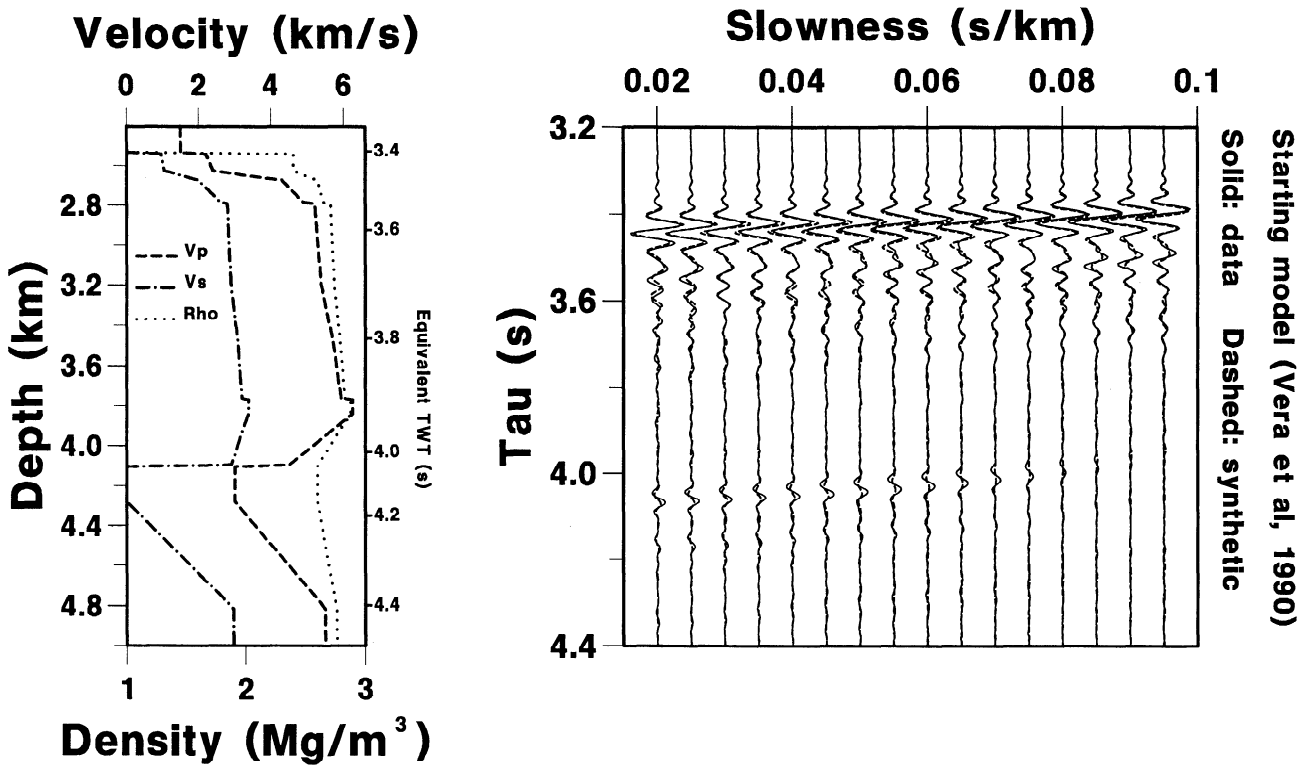

Figure 10. Assessment of the suitability of our chosen starting (long wavelength) velocity model devised from ESP data [*Vera et al.*, 1990] to the $\tau-p$ transformed gather. The seismic attenuation structure of the model is taken from *Vera et al.* [1990].

sion. In Figure 12 we compare the results obtained. Of the models shown, Figure 12a, the pure melt model (Vs =0.0 km s^{-1} in the melt) gives the smallest misfit. Note that the misfit is larger than for the equivalent model shown in Figure 11 as more traces were used in its calculation. The fit at farthest offset for the Vs =0.0 km s^{-1} model, however, is not perfect: the phase is correctly modeled but the amplitudes are slightly higher. This is probably the result of oversimplified Vs structure, but we have no information in the data on which to base a more refined model of it. The partial melt models (Vs =1.0 and Vs =2.0 km s^{-1}) have comparatively larger misfits as they underpredict the amplitude decay with increasing slowness of the AMC. Note that the form of the three Vp inversions are almost identical, and all of these synthetics give a better match to the data than any of the previously suggested models shown in Figure 5.

All the models shown in Figure 12 have a density contrast between the roof and melt rocks of 0.1 Mg m^{-3}. As explained earlier, we did not expect the choice of density within the narrow range measured on basaltic rocks to have a strong influence on the inversion results. However, to illustrate this point, we reran the inversion with the same starting model as used in Figure 12a but with a density contrast of 0.2 Mg m^{-3}. The result can be seen in Figure 13. The effect of changing ρ in the melt has negligible effect on the inversion result.

The final parameter that was held constant in the models up to this point that needed investigation was Qp. In the modeling so far we adopted the Qp values derived by *Vera et al.* [1990] from the amplitude with range decay of turning arrivals in the ESP data (Qp=80 for the top 1 km of crust, 100 from a depth of 1 km to the top of the AMC and 50 in the melt). From the tomography data *Wilcock et al.* [1995] estimate Qp=35-70 in the top 1 km. In a third experiment with bottom shots and receivers, *Christeson et al.* [1994] estimate Qp=10-20 in the top 0.15-0.3 km (layer 2A) and Qp=70-100 below (layer 2B). Qp in basaltic melts is not well constrained by measurements because of a strong dependence on the sonic frequency at which it is measured. For example, *Manghnani et al.* [1986] report values between 15 and 260 for basalts with 5-9 MgO % wt at 1400°C measured between 10 and 3.4 MHz. To cover the extreme range of values that were feasible, we decided to run inversions with models in which we halved and doubled Qp of the Vera model (Figure 14). Comparatively higher attenuation in the low Qp model means that a bigger acoustic impedance contrast is needed at the top of the low-velocity zone (more than 2.5 km s^{-1} compared to 2.0 km s^{-1}) to produce the observed AMC amplitude. The extra attenuation in the melt (Qp=25) results in the floor of the sill being less gradational. In comparison, doubling Qp has negligible effect on the inverted model.

As a final demonstration of the improvement in the fit to the data, we approximated our inversion results of AMC structure with a simplified velocity model, assumed the upper crustal structure to be as the Vera

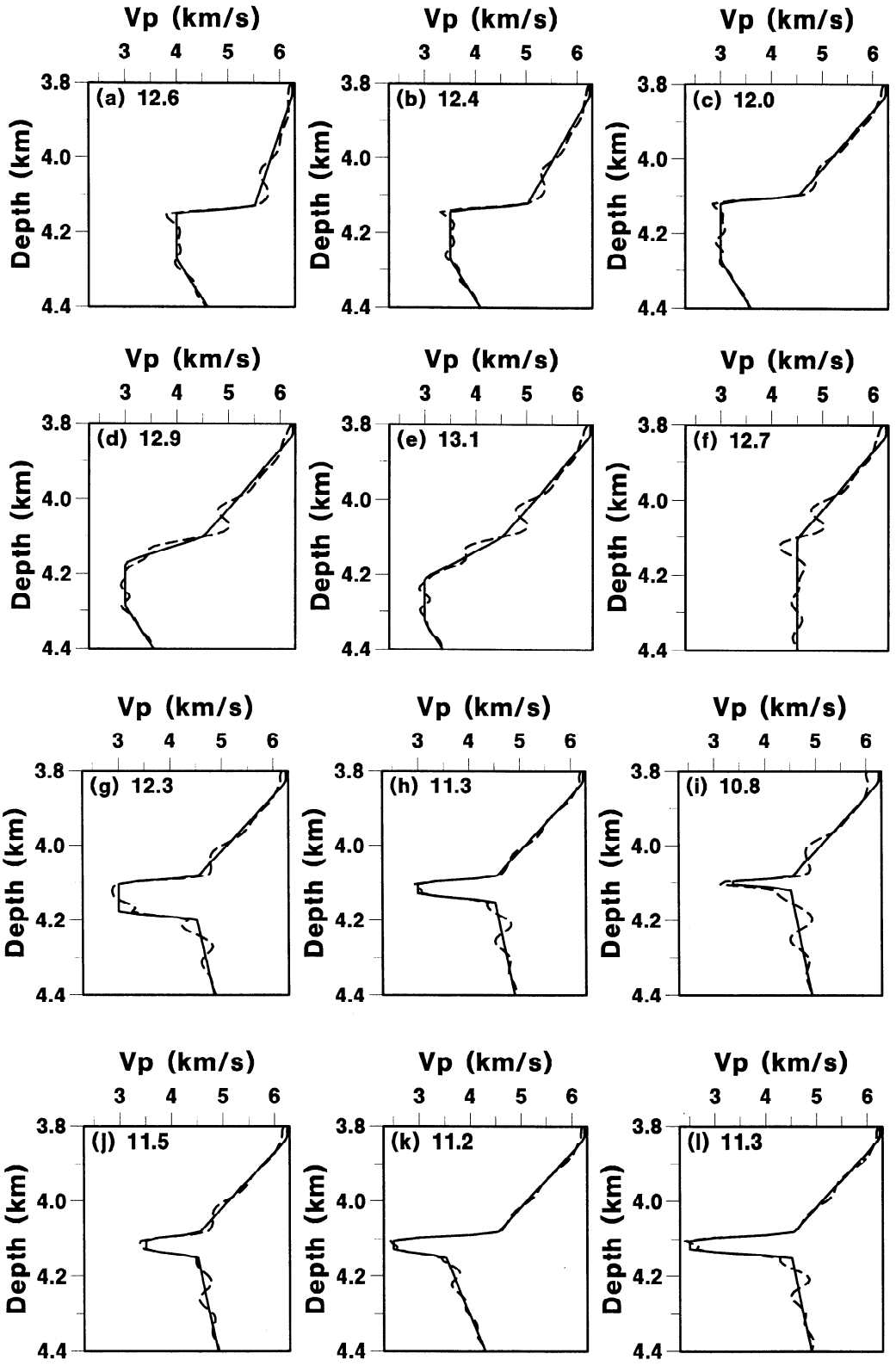

Figure 11. Starting (solid line) and final (dashed line) velocity models. The number in the top left-hand corner is misfit in arbitrary units (smaller misfits imply a better fit to the data). (a-c) Models with different velocity immediately above the AMC (5.5, 5.0 and 4.5 km s^{-1}, respectively); (d-f) models with different velocity gradients at the top of the AMC. Note that all these give bigger misfits than model c; (g-i) models of molten sills of different thickness (100, 50 and 20-m, respectively); (j-l) models of molten sills with different velocities in the sill and floor rocks (3.5 and 4.5, 2.5 and 3.5, 2.5 and 4.5 km s^{-1}, respectively); (m-o) models with different velocity gradients below the AMC. Note that including a gradient below the AMC reduces the misfit compared to a sharp contrast like models g-l.

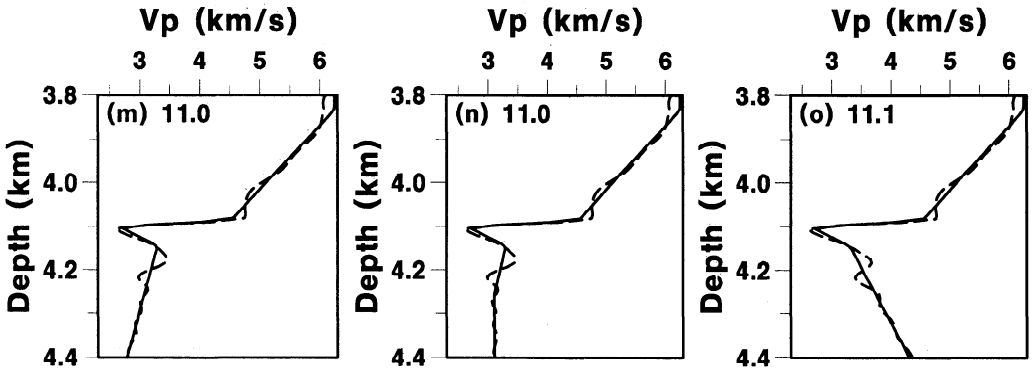

Figure 11. (continued)

model and forward modeled the response (Figure 15a). The results are therefore directly comparable with those of the previously proposed AMC models shown in Figure 5. Note that the misfit is larger than for our inverted solutions as it includes misfit of the upper crustal reflectivity. Our final model has Vp =2.6 km s^{-1} in the melt lens which has a thickness of 30 m. It is underlain by a velocity gradient in which Vp increases from 2.6 to 3.5 km s^{-1} over a vertical distance of 50 m. Figure 15b demonstrates that this gradient is required by the data

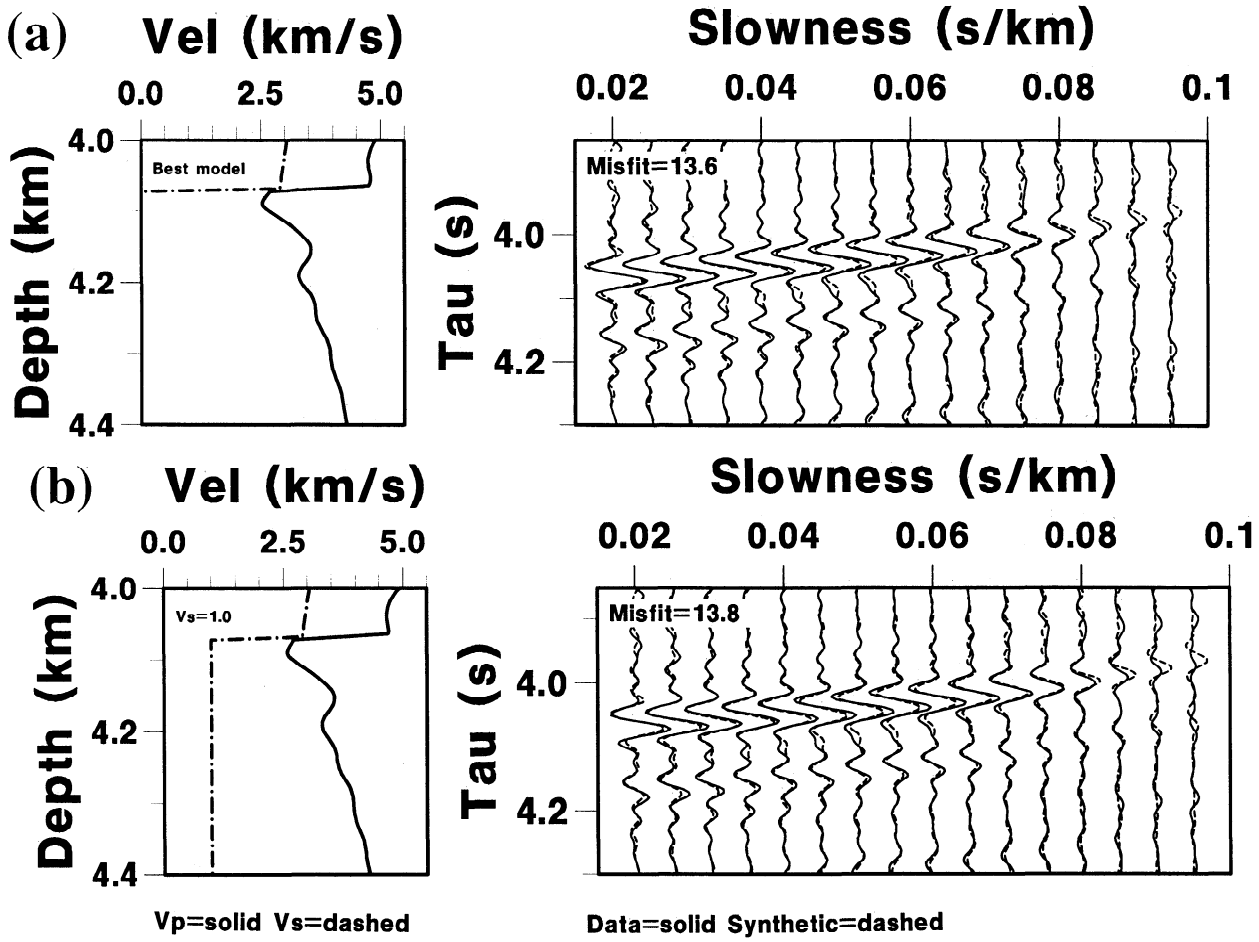

Figure 12. Vp inversion results for different Vs values in the melt. (a) Vs =0.0, (b) Vs =1.0, and (c) Vs =2.0 km s^{-1}. The density contrast across the boundary is 0.1 Mg m^{-3} and the Qp structure is Qp=80 for the top 1000-m of crust, Qp=100 from 1000-m to the top of the AMC and Qp=50 below the AMC [*Vera et al.*, 1990].

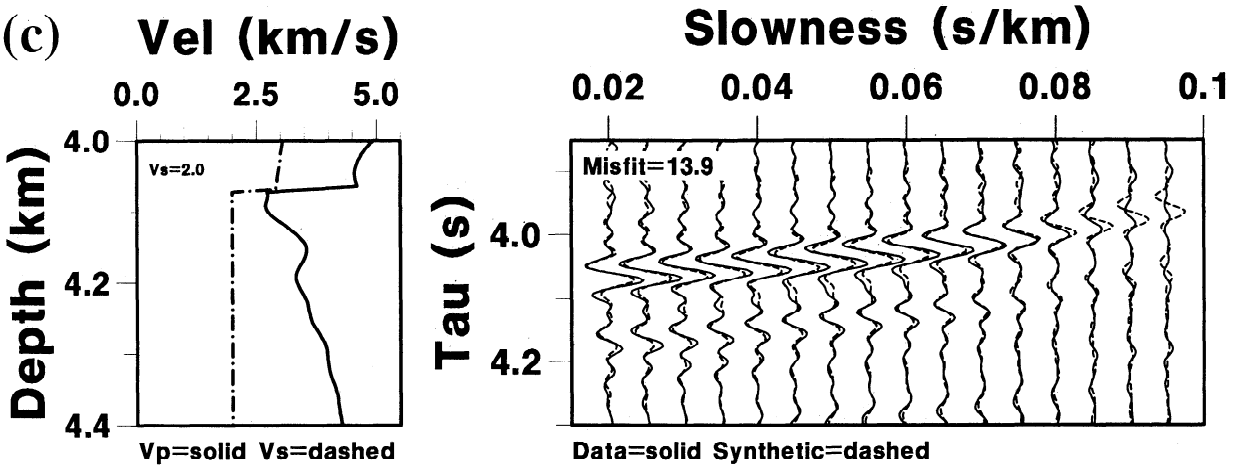

Figure 12. (continued)

if Qp in the melt is 50. Although not well constrained by the data we believe that Vs in the melt lens is not significantly different from 0.0 km s^{-1}.

Discussion

Having obtained a seismic velocity profile of the melt body beneath the ridge axis at 9°N, we want to interpret our results in terms of melt content. First we made comparisons with the experimental results of *Murase and McBirney* [1973]. Note that these experiments were performed without confining pressure, and so the sharp drop in Vp at subsolidus temperatures is due to microcracking. Vp =3.5 km s^{-1} falls on this part of the curve, and so we do not use these experimental data to interpret it. However, Vp =2.6 km s^{-1} falls in the region of melting where the experimental data are more reliable and suggests, by comparison with temperature versus melt content data presented by *Sinton and Detrick* [1992], that melt with this seismic velocity contains about 40% melt. Our preferred method of estimating melt content was to compute Hashin-Shtrikman bounds as outlined in Appendix A. We plot our results in Figure 16. According to this method, Vp =2.6 km s^{-1} translates into a melt content of 70-90%, and Vp =3.5 km s^{-1} translates into a melt content of 30-65%. We therefore interpret our results as evidence for a 30-m mostly molten layer which grades downward into a crystalline mush zone. The data require crystallinity of 35-70% to be achieved in just 50 m downward. The shape of our velocity-depth profile implies that accretion of material to the roof of the sill is minor and that crystal settling under gravity is a far more important physical process. The top 30-m low-Vp layer could be due to thermal convection.

Our results lend additional support for the new model of the magma chamber beneath fast spreading ridge axes proposed by *Sinton and Detrick* [1992]. This model was devised from the combination of geophysical, geochemical and petrological data and shows a thin, narrow sill-like body of melt overlying a thicker, wider crystal mush zone. However, up until this point the vertical profile through the sill and mush zone has not been well constrained. The small size of the mostly molten

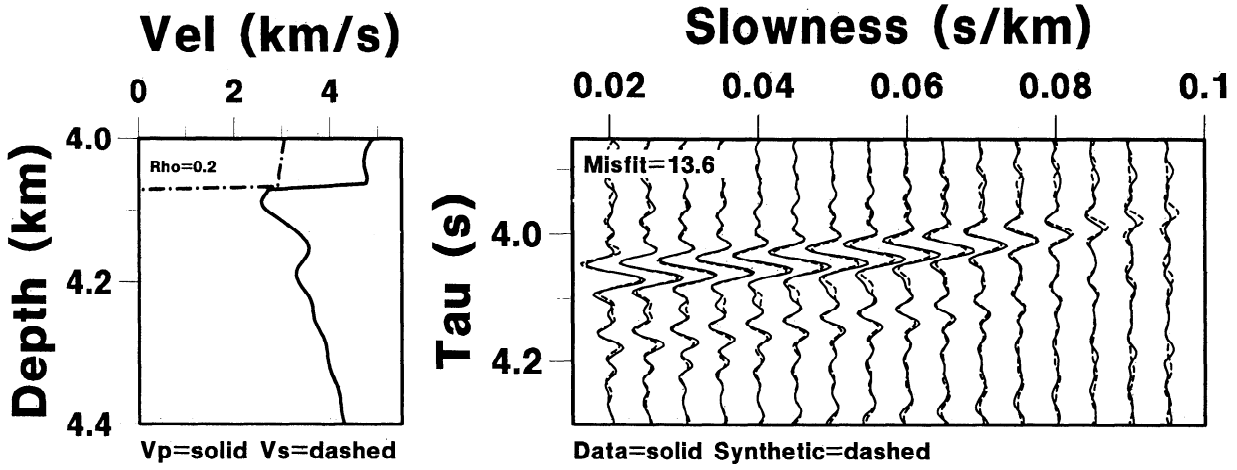

Figure 13. Vp inversion results with a density contrast of 0.2 Mg m^{-3} across the solid/melt interface. Other starting model parameters are as in Figure 12a.

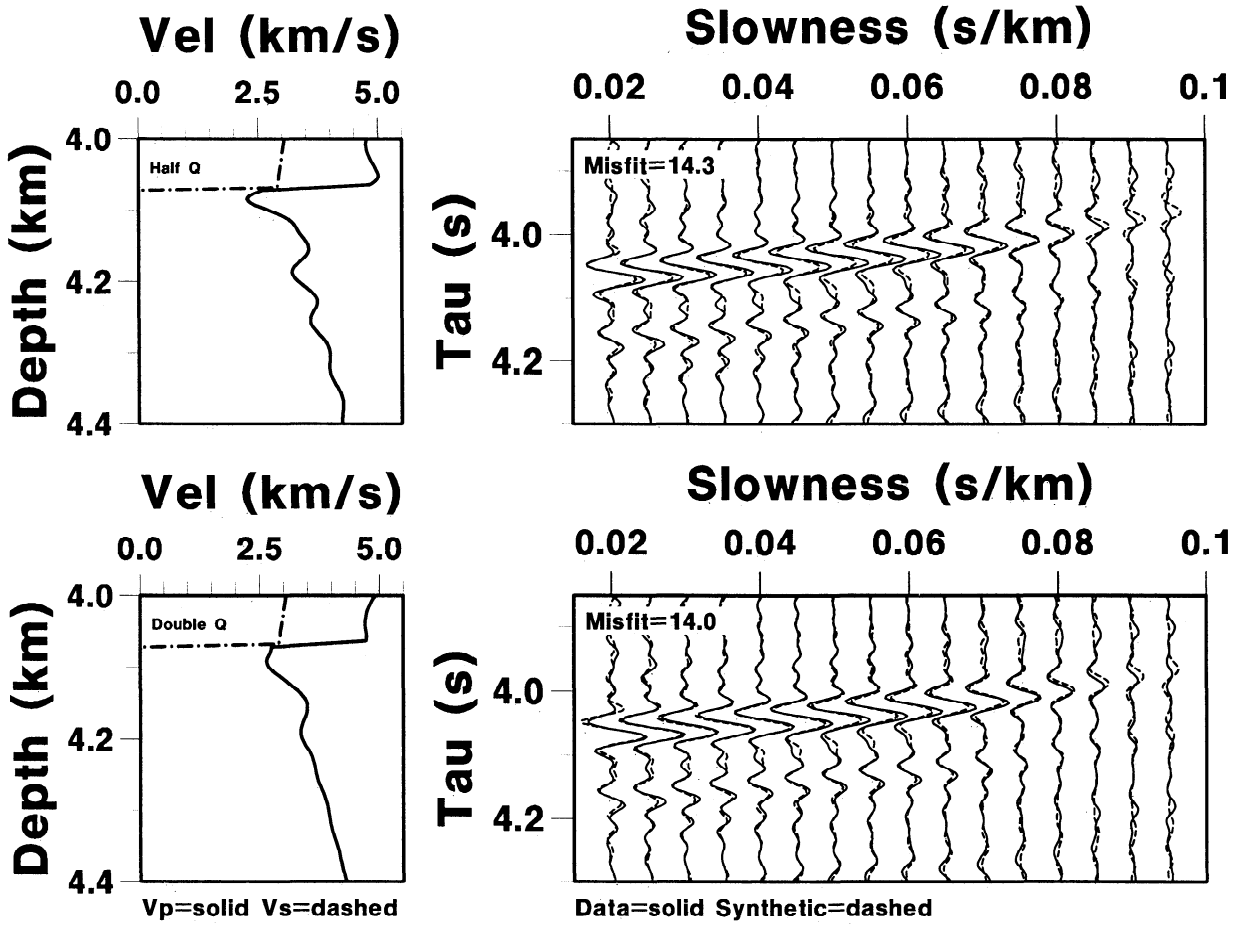

Figure 14. *Vp* inversion results for different *Qp* structure. We show two models, one in which *Qp* in every layer was double and another in which it was half the values used in the models shown in Figures 12 and 13. A lower *Qp* value means more seismic energy attenuation. Other starting model parameters are as in Figure 12a.

layer and its close contact to an increasing crystal content mushy zone detected in our study lends itself to the development of great variation in along-axis basalt geochemistry as seen in sampling studies [e.g., *Langmuir et al.*, 1986].

From studies of lava lakes, *Marsh* [1989] proposed that once crystallinity in a basaltic melt exceeds 25% it behaves rheologically like a solid and is unlikely to be erupted. This suggestion is consistent with the observation that samples collected at this part of the ridge axis tend to contain ~10% phenocrysts and implies that at the time of the seismic experiment only material from the 30-m-thick sill could be erupted. In fact, the portion of the ridge just north of our study area erupted in 1991, six years after the collection of the seismic data [*Haymon et al.*, 1993]. Unfortunately, the volume of material extruded at that time could not be estimated to enable us to make a direct volumetrical estimate. However, it demonstrates that this part of the ridge system was capable of erupting at this time, an observation that is consistent with our detection of low-*Vp*, low-*Vs* material at the top of the magma chamber. Most of the samples analyzed by *Batiza and Niu* [1992] contain only plagioclase phenocrysts. They ascribed this to gravitational crystal settling of mafic phases (olivine and clinopyroxene) and flotation of plagioclase. Our observation that crystals are compacting over length scales of a few tens of meters means that gravity filtering could occur over realistic timescales.

Obviously, our results are merely a snapshot in time of a particular part of the ridge system. We would expect the relative thicknesses of the convecting mostly molten part and the compacting crystalline part to change with time and place. Nonetheless, we believe our results to be a robust evaluation of the length scales under which solid-liquid fractionation is occurring within the magma chambers beneath fast spreading ridge axes.

Conclusions

We have rigorously applied waveform inversion to single-ship multichannel data collected at the East Pacific Rise near 9°N in order to determine the precise velocity structure of the melt body causing the AMC reflection. Our analysis supports the idea of a melt lens as previously suggested from forward modeling seismic data from this location. Our final model has *Vp* $=2.6\ \mathrm{km\,s^{-1}}$ in the melt lens which has a thickness of

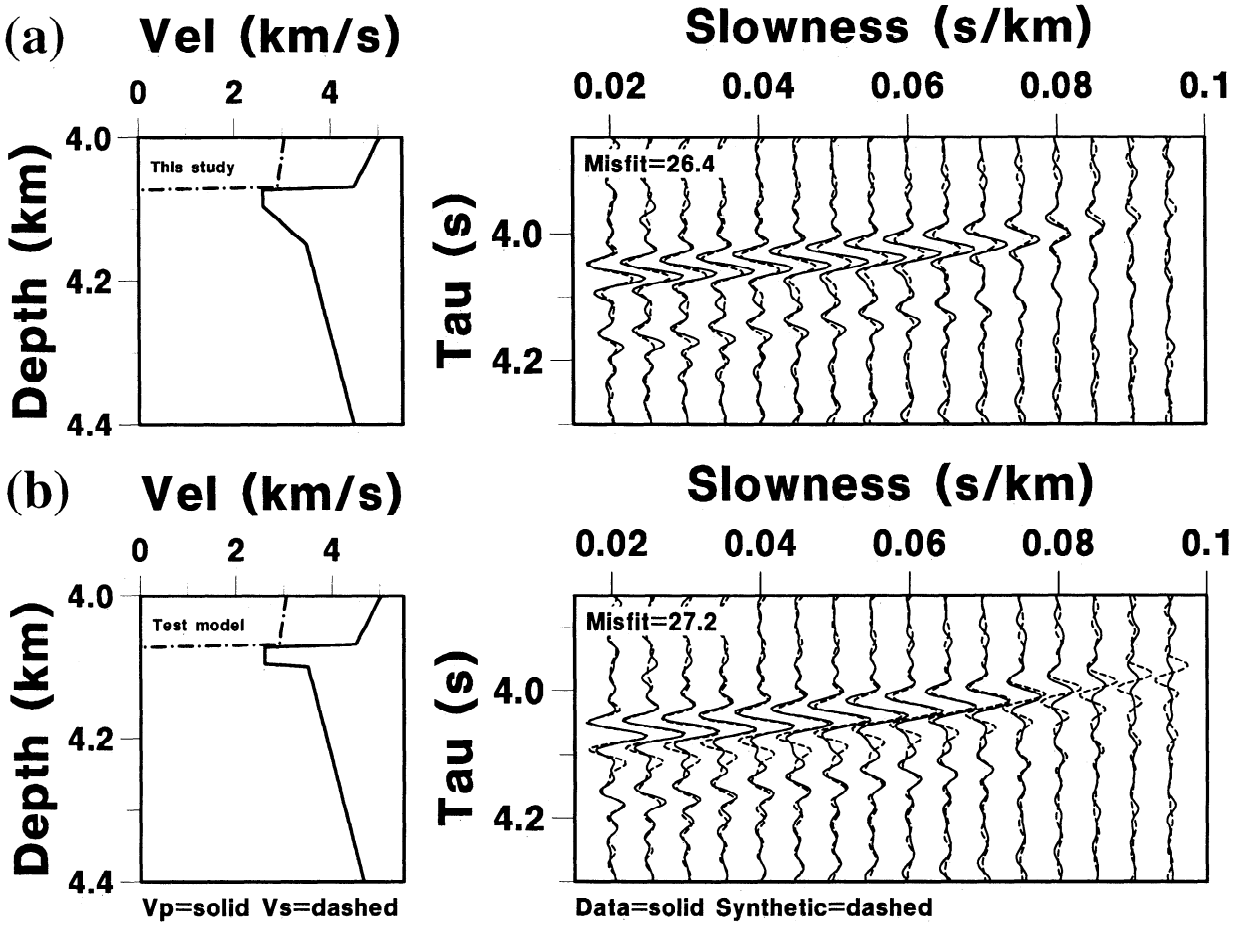

Figure 15. (a) Forward modeling results for AMC structure determined in this study. The velocity model is identical to those shown in Figure 5 at depths less than 4 km. The results of this study are therefore directly comparable with the results of the two earlier studies. Our final model has Vp =2.6 km s^{-1} in the melt lens which has a thickness of 30-m. It is underlain by a velocity gradient in which Vp increases from 2.6 to 3.5 km s^{-1} over a vertical distance of 50-m. Vs in the melt lens is not significantly different from 0.0 km s^{-1}. (b) Artificially modified model showing worsening of fit if floor gradient is replaced by first-order discontinuity.

30-m. It is underlain by a velocity gradient in which Vp increases from 2.6 to 3.5 km s^{-1} over a vertical distance of 50-m. Although not well constrained by the data we believe that Vs in the melt lens is not significantly different from 0.0 km s^{-1}. We suggest that only material from the 30-m-thick lens can erupt. The underlying velocity gradient zone may represent crystal settling under gravity.

Appendix A: Calculation of Seismic Velocity—for a Two Phase Medium

For a two-phase material, *Hashin and Shtrikman* [1963] showed that bounds can be placed on its effective elastic properties depending on the textural relationship of the two phases. In our situation the maximum bound occurs for the case where the material consists of unconnected melt inclusions in a solid matrix and the minimum bound where the material consists of unconnected crystals in a molten host. For this case the composite bulk and shear moduli for the upper (κ^{HS+}, μ^{HS+}) and lower (κ^{HS-}, μ^{HS-}) Hashin-Shtrikman bounds are given by

$$\kappa^{HS+} = \kappa_s - \frac{\nu_m P_s(\kappa_s - \kappa_m)}{P_s - (1-\nu_m)(\kappa_s - \kappa_m)} \quad \text{(A1)}$$

$$\kappa^{HS-} = \frac{\kappa_s \kappa_m}{\nu_m \kappa_s + (1-\nu_m)\kappa_m} \quad \text{(A2)}$$

$$\mu^{HS+} = \frac{5(1-\nu_m)P_s\mu_s}{5P_s - 2\nu_m(\kappa_s + 2\mu_s)} \quad \text{(A3)}$$

$$\mu^{HS-} = 0 \quad \text{(A4)}$$

where κ_s and μ_s are the bulk and shear moduli of the solid crystals, κ_m and μ_m are the bulk and shear moduli of the fluid melt, ν_m is the melt concentration and $P_s = \kappa_s + 4/3\mu_s$. Note that this theory assumes both phases are assumed isotropic, but the bounds are not influenced by the shape of the inclusions.

The minimum and maximum P and S wave velocities can then be calculated from the composite bulk and shear moduli bounds using

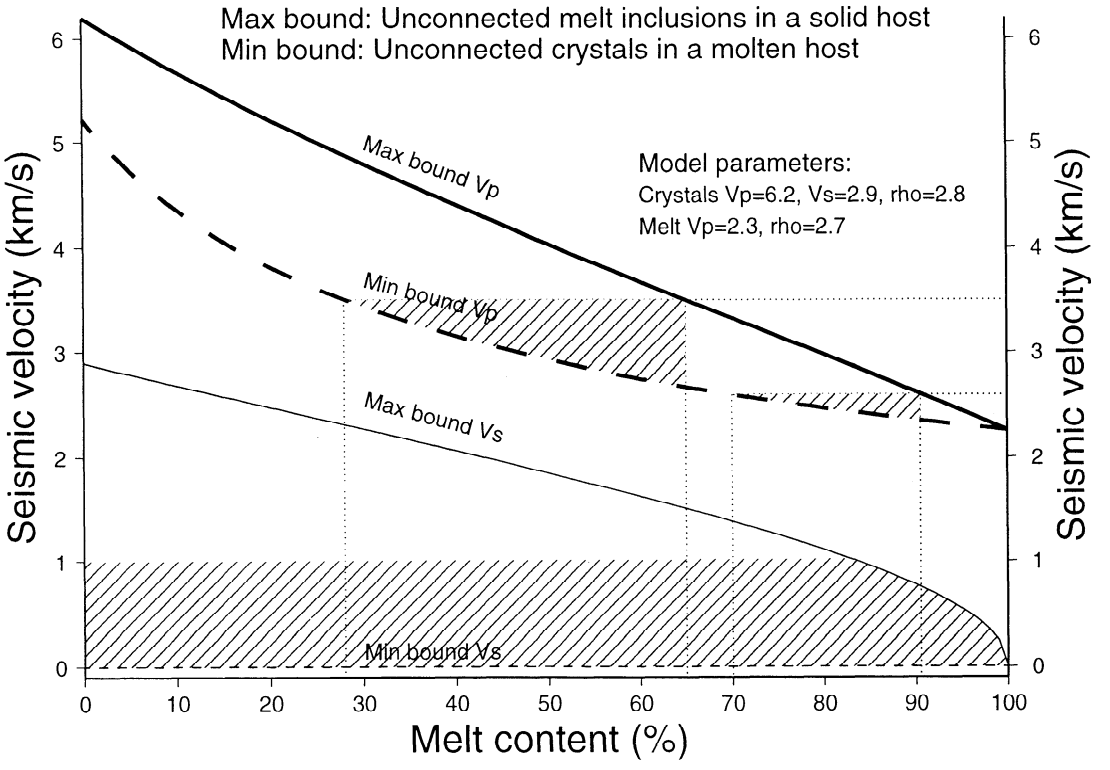

Figure 16. Hashin-Shtrikman bounds on seismic velocity for a two-phase material (in our case, melt and crystals). The dotted lines are drawn at Vp =2.6 and 3.5 $\mathrm{km\,s^{-1}}$, critical velocities in our final inverted model (Figure 15).

$$Vp = \sqrt{\frac{\kappa + \frac{4}{3}\mu}{\rho}} \tag{A5}$$

$$Vs = \sqrt{\frac{\mu}{\rho}} \tag{A6}$$

Acknowledgments. We are grateful to Bob Detrick for providing us with the data used in this study and to Graham Kent for proving an estimate of the source wavelet. We would also like to thank Francoise Kormendi and Michel Dietrich for providing us with their inversion code and Richard Hobbs for help with computational implementation and insight into source wavelets. An earlier draft was improved by comments made by Mrinal Sen, George Sutton and an anonymous reviewer. J.S.C. acknowledges receipt of a BRIDGE (NERC) fellowship.

References

Batiza, R., and Y. Nui, Petrology and magma chamber processes at the East Pacific Rise ~ 9°30′N, *J. Geophys. Res., 97*, 6779-6797, 1992.

Christeson, G.L., W.S.D. Wilcock, and G.M. Purdy, The shallow attenuation structure of the fast-spreading East Pacific Rise near 9°30′N, *Geophys. Res. Lett., 21*, 321-324, 1994.

Detrick, R.S., P. Buhl, E.E. Vera, J.C. Mutter, J.A. Madsen, and T.M. Brocher, Multi-channel seismic imaging of a crustal magma chamber along the East Pacific Rise, *Nature, 326*, 35-41, 1987.

Harding, A.J., Slowness-time mapping of near-offset seismic reflection data, *Geophys. J. R. Astron. Soc., 80*, 463-492, 1985.

Haymon, R.M., et.al. Volcanic eruption of the mid-ocean ridge along the East Pacific Rise crest at 9°45′ – 52′N: Direct submersible observations of the seafloor phenomena associated with an eruption in April 1991, *Earth Planet. Sci. Lett., 119*, 85-101, 1993.

Hashin, Z., and S. Shtrikman, A variational approach to the theory of the elastic behaviour of multiphase materials, *J. Mech. Phys. Solids, 11*, 127-140, 1963.

Herron, T.J., P.L. Stoffa, and P. Buhl, Magma chamber and mantle reflections: East Pacific Rise, *Geophys. Res. Lett., 7*, 989-992, 1980.

Kappus, M.E., A.J. Harding, and J.A. Orcutt, A comparison of tau-p transform methods, *Geophysics, 55*, 1202-1215, 1990.

Kennett, B.L.N., *Seismic Wave Propagation in Stratified Media*, Cambridge Univ. Press, New York, 1983.

Kennett, B.L.N., and N.J. Kerry, Seismic waves in a stratified half-space, *Geophys. J. R. Astron. Soc., 57*, 557-583, 1979.

Kent, G.M., A.J. Harding, and J.A. Orcutt, Evidence for a smaller magma chamber beneath the East Pacific Rise at 9°30′N, *Nature, 344*, 650–653, 1990.

Kent, G.M., A.J. Harding, and J.A. Orcutt, Distribution of magma beneath the East Pacific Rise between the Clipperton transform and the 9°17′N Deval from forward modeling of common depth point data, *J. Geophys. Res., 98*, 13945-13969, 1993a.

Kent, G.M., A.J. Harding, and J.A. Orcutt, Distribution of magma beneath the East Pacific Rise near the 9°03′N overlapping spreading center from forward modeling of common depth point data, *J. Geophys. Res., 98*, 13971-13995, 1993b.

Korenaga, J., W.S. Holbrook, S.C. Singh, and T.A. Minshull, Natural gas hydrates on the southeast U.S. margin: Constraints from full waveform inversion and travel time inversion of wide-angle seismic data, *J. Geophys. Res., 102*, 15,345-15,365, 1997.

Kormendi, F., and M. Dietrich, Non-linear waveform inversion of plane-wave seismograms in stratified elastic media, *Geophysics, 56*, 664–674, 1991.

Langmuir, C.H., J.F. Bender, and R. Batiza, Petrological and tectonic segmentation of the East Pacific Rise, 5°30′ – 14°30′N, *Nature, 332*, 422-429, 1986.

Laws, R.M., L. Hatton, and M. Haartsen, Computer modeling of clustered air guns, *First Break, 8*, 331–344, 1990.

Manghnani, M.H., H. Sato, and C.S. Rai, Ultrasonic velocity and attenuation measurements on basalt melts to 1500°C: Role of composition and structure in the viscoelastic properties, *J. Geophys. Res., 91*, 9333-9342, 1986.

Marsh, B.D., Magma chambers, *Annu. Rev. Earth Planet. Sci., 17*, 439-474, 1989.

Minshull, T.A. and S.C. Singh, Shallow structure of oceanic crust in the western North Atlantic from seismic waveform inversion and modeling, *J. Geophys. Res., 98*, 1777-1792, 1993.

Murase, T., and A.R. McBirney, Properties of some common igneous rocks and their melts at high temperature, *Geol. Soc. Am. Bull., 84*, 3563-3592, 1973.

Mutter, J.C., G.A. Barth, P. Buhl, R.S. Detrick, J.A. Orcutt, and A.J. Harding, Magma discontinuities across ridge-axis discontinuities on the East Pacific Rise from multichannel seismic images, *Nature, 336*, 156-158, 1988.

Oppenheim, A.V. and R.W. Schafer, *Digital Signal Processing*, Prentice-Hall, Englewood Cliffs, N.J., 1975.

Singh, S.C., G.F. West, and C.H. Chapman, On plane-wave decomposition: Alias removal, *Geophysics, 54*, 1339-1343, 1989.

Singh, S.C., M. Dietrich, and F. Chapel, A complete waveform inversion and its application to ECORS data, in *Continental Lithosphere: Deep Seismic Reflections, Geophys. Ser.*, vol.22, edited by R. Meissner, et al., pp. 391–400, AGU, Washington, D. C., 1991.

Singh, S.C., T.A. Minshull, and G.D. Spence, Velocity structure of a gas hydrate reflector, *Science, 260*, 204–206, 1993.

Sinton, J.M. and R.S. Detrick, Mid-ocean ridge magma chambers, *J. Geophys. Res.*, 97, 197-216, 1992.

Tarantola, A., A strategy for nonlinear inversion of seismic reflection data, *Geophysics, 51*, 219-232, 1986.

Toomey, D.R., G.M. Purdy, S.C. Solomon, and W.S.D. Wilcock, The three-dimensional seismic velocity structure of the East Pacific Rise near latitude 9°30′N, *Nature, 347*, 639-645, 1990.

Toomey, D.R., S.C. Solomon, and G.M. Purdy, Tomographic imaging of the shallow crustal structure of the East Pacific Rise 9°30′N, *J. Geophys. Res., 99*, 24135-24157, 1994.

Vera, E.E., and J.B. Diebold, Seismic imaging of oceanic layer 2A between 9°30′N and 10°N on the East Pacific Rise from 2-ship wide-aperture profiles, *J. Geophys. Res., 99*, 3031-3041, 1994.

Vera, E.E., J.C. Mutter, P. Buhl, J.A. Orcutt, A.J. Harding, M.E. Kappus, R.S. Detrick, and T.M. Brocher, The structure of 0-0.2 My old oceanic crust at 9°N on the East Pacific Rise from expanded spread profiles, *J. Geophys. Res., 95*, 15529-15556, 1990.

Wilcock, W.S.D., S.C. Solomon, G.M. Purdy, and D.R. Toomey, Seismic attenuation structure near 9°30′N, *J. Geophys. Res., 100*, 24,147-24,165, 1995.

Ziolkowski, A., Why don't we measure seismic signatures?, *Geophysics, 56*, 190-201, 1991.

J.S. Collier and S.C. Singh, Bullard Laboratories, Department of Earth Sciences, University of Cambridge, Madingley Road, Cambridge, CB3 OEZ. England. (email: collier@esc.cam.ac.uk; singh@esc.cam.ac.uk)

(Received November 27, 1996; revised May 17, 1997; accepted May 21,1997.)